

Solution of the Euler equations on unstructured grids for two-dimensional compressible flow

ABSTRACT

A method for the numerical solution of the two-dimensional Euler equations on unstructured grids has been developed. The cell-centred symmetric finite-volume spatial discretisation is applied in a general formulation that allows the use of arbitrary polygonal computational cells. The integration in time, to a steady-state solution, is performed using an explicit, multi-stage procedure, with standard convergence acceleration techniques such as local time stepping, enthalpy damping and implicit residual smoothing. Accuracy of solution, in terms of minimising spurious entropy production, is achieved through careful treatment of the artificial dissipative terms near boundaries. Standard test cases for both subcritical and supercritical flow, including single- and multi- element aerofoils have used to validate the method.

1. NOTATION

C_L, C_D	lift and drag coefficients
c	speed of sound
D_k	discretised dissipative flux integral
$d^{(2)}, d^{(4)}$	dissipative fluxes
E	total energy per unit mass
F, G	flux vectors
H	total enthalpy per unit mass
$k^{(2)}, k^{(4)}$	coefficients of the dissipative fluxes
P	static pressure
Q_k	discretised flux integral
R_k	residual
S	boundary of Ω
t	time
U, V	Cartesian velocity components
W	vector of conserved variables
x, y	Cartesian coordinates
α	scaling factor
γ	ratio of specific heats
Δt	time step
ε	coefficient for implicit residual smoothing
$\varepsilon^{(2)}, \varepsilon^{(4)}$	coefficients for dissipative terms
V	shock sensor

ρ	density
σ	coefficient for enthalpy damping
Ω	volume of domain

2. INTRODUCTION

Analysis methods based on the numerical solution of the Euler equations for inviscid compressible flow can be used to predict some of the aerodynamic characteristics of aerofoils at high Reynolds number. A number of existing methods are quite accurate and robust, but are usually restricted to simple geometrical configurations such as single aerofoils. The main problems involved with the analysis of more complex geometries, such as the multi-element aerofoils associated with mechanical high-lift systems are concerned with the generation of a suitable computational grid. This is due to the multiply-connected nature of such geometries.

Two alternative grid-generation techniques have been proposed to overcome these problems: the structured multi-block approach and the unstructured approach. The multi-block method divides the entire complex domain into several simple domains (or blocks), and a structured grid based on quadrilateral cell is generated in each block using standard single-block techniques involve the use of triangular or polygonal cells, and the grid-points can be distributed using a number of suitable algorithms.

The structured multi-block approach requires several compatibility conditions at each block interface (such as point and slope continuity), and the decomposition of the flow domain into blocks is relatively difficult to automate. However, the quality of the resulting grids can be very high, and the presence of body-fitted coordinate lines near solid boundaries aids the development of accurate flow solvers. On the other hand, unstructured grids can be made to fit very complex geometries in a relatively straightforward manner, since the distribution of grid points can be done in a completely

arbitrary way. Furthermore, it is possible to develop unstructured flow solvers that are able to deal with regions of structured grid, such regions being simply treated in an unstructured manner. However, an unstructured flow solver is, in general, computationally slow, due to the requirement for indirect addressing of data. This does not allow the best use to be made of the architecture of vector computers. The optimum approach is probably to use a hybrid flow solver, as proposed by Weatherill, but this essentially means that both an unstructured and a structured flow solver need to be implemented within the same numerical scheme.

In the present work, a time-marching solution method for the Euler equations governing two-dimensional inviscid compressible flow is developed. The flow algorithm solves the time-dependent integral form of the equations by means of a cell-centred, symmetric finite-volume spatial discretisation. The integration in time, to a steady-state solution, is performed using an explicit multi-stage procedure. The algorithm works in terms of cell edges, rather than the cells themselves, and the cells can be polygons of an arbitrary number of sides. In this way, complex geometries can be treated with hybrid structured/unstructured grids (all treated as unstructured, however). The approach provides a natural framework for the implementation of grid-refinement and flow-adaptation techniques, without the need to modify the basic flow algorithm.

Extensive numerical studies have been performed in order to assess the accuracy of the present approach. Accurate solutions have been achieved by paying special attention to the treatment of the artificial dissipation terms (used to damp spurious oscillatory solution modes) near the boundaries of the computational domain. The resulting inviscid-flow solver is to form the basis for the development of a viscous-flow solver, based on a solution of the Reynolds-averaged Navier-Stokes equations. For such a solver, the ability to treat regions of structured grid near solid boundaries, within an overall unstructured framework, may be advantageous for the implementation of turbulence models.

3. GOVERNING FLOW EQUATIONS

The Euler equations are the expression of the conservation principle for mass, momentum and energy. In a two-dimensional domain of volume Ω with boundary S , the equations may be written in the following form

$$\frac{\partial}{\partial t} \int_{\Omega} W d\Omega + \int_S (F dy - G dx) = 0 \quad (1)$$

where x and y are Cartesian coordinates. W is the vector of conserved variables.

$$W = \begin{bmatrix} \rho \\ \rho U \\ \rho V \\ \rho E \end{bmatrix} \quad (2)$$

and F, G are flux vectors

$$F = \begin{bmatrix} \rho U \\ \rho U^2 + P \\ \rho UV \\ \rho UH \end{bmatrix}, G = \begin{bmatrix} \rho V \\ \rho UV \\ \rho V^2 + P \\ \rho VH \end{bmatrix} \quad (3)$$

The contour integration around S is taken in the anticlockwise sense.

ρ, P, H and E are the density, pressure, total enthalpy per unit mass and total energy per unit mass respectively; U and V are the Cartesian components of the velocity vector. These quantities are related to each other by the definitions of total energy per unit volume and total enthalpy per unit volume for a perfect gas

$$\rho E = P / (\gamma - 1) + \rho(U^2 + V^2) / 2 \quad (4)$$

$$\rho H = \rho E + P \quad (5)$$

4. FINIT-VOLUME SPATIAL DISCRETISATION

4.1 General Formulation

The computational domain is divided into a finite number of non-overlapping cells, and the integral conservation equations are applied to each cell. Since the volume of any cell is supposed to be constant with respect to time, equation (1) can be written as

$$\frac{\partial W}{\partial t} = - \frac{\int_S (Fdy - Gdx)}{\int_{\Omega} d\Omega} \quad (6)$$

where Ω and S now refer to a cell, and W contains cell-average values. The time-dependent integral form of these equations suggests performing the spatial discretisation using a finite-volume technique, and then marching the resulting semi-discrete equations in time to reach the steady-state solution.

Performing the spatial discretisation of equation (6) before the time discretisation (the so-called method of lines) leads to a large set of ordinary differential equations with respect to time

$$\frac{dW_k}{dt} = - \frac{Q_k}{\Omega_k} \quad (7)$$

Where Ω_k is the volume of the kth cell and W_k is the vector of conserved variables. Q_k is a discrete approximation of the flux integral, the right-hand side of equation(6), and is given by

$$Q_k = \sum_{i=1}^{kedges} (F\Delta y_i - G\Delta x_i) \quad (8)$$

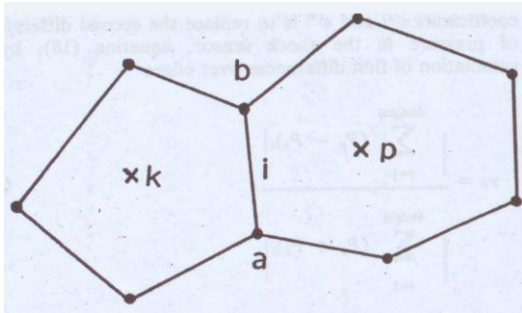


Figure 1. Nomenclature for cell centres, edges and grid vertices.

where

$$\Delta x_i = x_b - x_a, \Delta y_i = y_b - y_a \quad (9)$$

and the summation is over the edges (kedges) forming the kth cell. Using the cell-centred finite-volume approach, in which the

conserved variables are located at the centres of cells, the flux across the ith edge is calculated using simple averages of variables at the two neighbouring cell centres k and p (see Fig. 1), e.g.

$$W_i = (W_k + W_p) / 2 \quad (10)$$

Introducing

$$Z_i = U_i \Delta y_i - V_i \Delta x_i \quad (11)$$

The Euler equations in discrete form applied to cell **k**, equation(7), become

$$\frac{dW_k}{dt} = - \frac{1}{\Omega_k} \sum_{i=1}^{kedges} \begin{bmatrix} Z\rho \\ Z\rho U + P\Delta y \\ Z\rho V - P\Delta x \\ Z\rho H \end{bmatrix} \quad (12)$$

The above general formulation can be used for structured as well as for unstructured grids. The only difference is that, in the former case, equation (12) can be written in a more compact form because, using curvilinear coordinates, each cell is identified by a two-index matrix. An extensive discussion for structured grids can be found in the original paper of Jameson et al Ref. (2) or in Refs (3) and (7).

4.2 Unstructured Approach

Unstructured grids cannot be represented in the same way as structured grids since there is not a grid-point matrix in which the neighbouring elements are the neighbouring points in the physical plane. For unstructured grids, a connectivity matrix is required, in which all the necessary information (such as coordinates of the grid vertices, number of edges, number of cells, etc.) is stored. This information is accessed in an indirect way by the flow solver, so the choice of an optimal scheme for data storage becomes important. In the present work, a cell-centred finite-volume approach is adopted, in order to reduce the amount of connectivity information to be Stored.

The connectivity matrix is written in terms of cell edges rather than the cells themselves. Therefore, each line of this matrix contains the information about one edge: the number of the edge, the numbers of the two adjacent cells,

and the numbers of the two vertices forming the edge. Following this procedure, the required connectivity information results in a matrix with dimensions (number of edges, 4). Since the scheme works in terms of edges, cells with arbitrary shape can be treated, with different cell shapes being allowed within the same grid. The only restriction is that the connectivity matrix should be constructed in a suitable way. Thus, the numbering system must preserve the anticlockwise sense, and the boundary edges (solid surface edges and outer boundary edges) must be separated from the interior edges. In the connectivity matrix (connmatrix), each edge is present only once, and calculations are performed with a do-loop over all edges, so that quantities are accumulated.

The structure of this very simple do-loop is illustrated in the following sequence of logical instructions

```

do i=1 , nedges
  k = connmatrix(i, 1)
  a = connmatrix(i, 2)
  b = connmatrix(i, 3)
  p = connmatrix(i, 4)
  flux = function(k, a, b, p)
  sum(k) = sum(k) + flux
  sum(p) = sum(p) - flux
end do

```

Here, the quantity of interest 'flux' is a function of the two adjacent cells (k and p) and of the two vertices defining the edge (a and b). The fluxes are accumulated in the array 'sum' following the conservative principle (i.e. 'flux' is added to cell k and subtracted from cell p).

This same do-loop can be used for the calculation of all quantities of interest: fluxes, cell areas, time steps, artificial dissipation terms etc. Since the do-loop works only in terms of edges, it is easy to see that the structure of the flow solver becomes independent of the actual cell shape.

5. ARTIFICIAL DISSIPATION

Cell-centred schemes such as the one described above are non-dissipative, so that any errors (discretisation errors, round-off error etc.) are not damped and oscillations may be present in the steady-state solution. In

order to eliminate these oscillations, artificial dissipative terms are added to the right-hand side of equation (7) which, for cell k, becomes

$$\frac{dW_k}{dt} = -(Q_k - D_k) / \Omega_k \quad (13)$$

In the present work, the approach of Jameson et al is adopted and the dissipation function D_k is constructed as a blending of second and fourth differences of the conserved variables W_k . The part involving fourth differences is added everywhere in the flow domain where the solution is smooth, but is switched-off in the region of shock waves. A term involving second differences is then switched-on to damp oscillations near shock waves, which can be very large. This switching is achieved by means of a shock sensor based on the local second differences of pressure.

5.1 Structured formulation

Jameson et al construct the artificial dissipative terms, for structured grids, as follows

$$D_{i,j} = (D^\xi + D^\eta)_{i,j} \quad (14)$$

where D^ξ and D^η are components with respect to the curvilinear coordinates ξ and η . Since the grid is structured, the cell centres are defined by the two indices i, j in these coordinate directions. The two components of equation(14) are written in terms of differences of cell-edge values

$$D_{i,j} = d_{i+1/2,j} - d_{i-1/2,j} + d_{i,j+1/2} - d_{i,j-1/2} \quad (15)$$

which, in turn, are composed of second and fourth differences of the conserved variables W, e.g.

$$d_{i+1/2,j} = d_{i+1/2,j}^{(2)} + d_{i+1/2,j}^{(4)} \quad (16)$$

with

$$d_{i+1/2,j}^{(2)} = \alpha_{i+1/2,j} \mathcal{E}^{(2)}(W_{i+1,j} - W_{i,j}) \quad (17a)$$

$$d_{i+1/2,j}^{(4)} = -\alpha_{i+1/2,j} \mathcal{E}^{(4)}(W_{i+2,j} - 3W_{i+1,j} + 3W_{i,j} - W_{i-1,j})$$

$$\dots\dots\dots (17b)$$

$\mathcal{E}^{(2)}$ and $\mathcal{E}^{(4)}$ are adaptive coefficient, which are switched on or off by use a shock-wave sensor ν

$$\nu_{i,j} = \frac{|P_{i+1,j} - 2P_{i,j} + P_{i-1,j}|}{|P_{i+1,j} + 2P_{i,j} + P_{i-1,j}|} \quad (18)$$

Finally, α is a scaling factor, which is defined in equation (26) below.

5.2 Unstructured formulation

Construction of the artificial dissipative terms for unstructured grids basically follows the above procedure. However, the resulting form of the adaptive coefficients is somewhat different. Within the finite-volume approach, the dissipation function for unstructured grids is calculated by a summation of the fluxes across the edges

$$D_k = \sum_{i=1}^{kedges} d_i^{(2)} + \sum_{i=1}^{kedges} d_i^{(4)} \quad (19)$$

Also, for unstructured grids, the second and fourth differences of conserved variables, equations (17), are replaced by

$$d_i^{(2)} = \alpha_i \varepsilon_i^{(2)} (W_p - W_k)_i \quad (20a)$$

$$d_i^{(4)} = -\alpha_i \varepsilon_i^{(4)} (\nabla^2 W_p - \nabla^2 W_k)_i \quad (20b)$$

Where index i denotes the edge delimiting cells k and p , and ∇^2 is defined as

$$\nabla^2 W_k = \sum_{j=1}^{kedges} (W_j - W_k) \quad (21)$$

The simplest way to determine the form of the adaptive coefficients $\varepsilon^{(2)}$ and $\varepsilon^{(4)}$ is to replace the second differences of pressure in the shock sensor, equation (18), by a summation of first differences over edges

$$\nu_k = \frac{\left| \sum_{i=1}^{kedges} (P_p - P_k)_i \right|}{\left| \sum_{i=1}^{kedges} (P_p + P_k)_i \right|} \quad (22)$$

The resulting adaptive coefficients are

$$\begin{aligned} \varepsilon_i^{(2)} &= k^{(2)} \max(\nu_p, \nu_k)_i \\ \varepsilon_i^{(4)} &= \max(0, k^{(4)} - \varepsilon_i^{(2)}) \end{aligned} \quad (23)$$

Where $k^{(2)}$ and $k^{(4)}$ are two empirically-chosen constants, which typically have values in the range $1/256 < k^{(4)} < 1/32$ and $1/2 < k^{(2)} < 1.0$.

The above form for the artificial dissipation

terms was found to be not entirely satisfactory, although the accuracy of the scheme is preserved. The reason seems to be associated with the isotropic behaviour of the shock sensor ν_k and the scaling factors α_i . By this is meant that there is only one shock sensor and scaling factor per edge. In a structured formulation, there would be two shock sensors and two scaling factors, corresponding to the two curvilinear coordinate directions.

In consequence, for the above unstructured formulation, the magnitude of the dissipative terms is too high in smooth regions and too low in regions where large gradients are present. After many complex but ineffective modifications, the following simple procedure has been adopted in the present work. The shock sensor and the scaling factor are constructed on an edge (i.e. local basis, using only flow variables from the two adjacent cells k and p)

$$\nu_i = \frac{|P_p - P_k|}{|P_p + P_k|} \quad (24)$$

The adaptive coefficients then become

$$\begin{aligned} \varepsilon_i^{(2)} &= k^{(2)} \nu_i \\ \varepsilon_i^{(4)} &= \max(0, k^{(4)} - \varepsilon_i^{(2)}) \end{aligned} \quad (25)$$

The scaling factor α_i is based on the maximum eigenvalues of the Jacobian matrices $\partial F / \partial W$ and $\partial G / \partial W$ along the appropriate cell edge

$$\alpha_i = |U \Delta y - V \Delta x| + c \sqrt{(\Delta x^2 + \Delta y^2)} \quad (26)$$

where U , V and c are average values on the dividing edge, c being the local speed of sound.

Incorrect treatment of the dissipation terms near boundaries (both solid surface and outer boundaries) can result in a significant loss in solution accuracy. The dissipation terms added to damp oscillations can be too strong and, locally, the order of the numerical scheme can be reduced. From a physical point of view, this strong dissipation produces a large amount of spurious numerical entropy near the boundary. This leads to pressure losses on the surface of the aerofoil, and so integrated loads will also be incorrect.

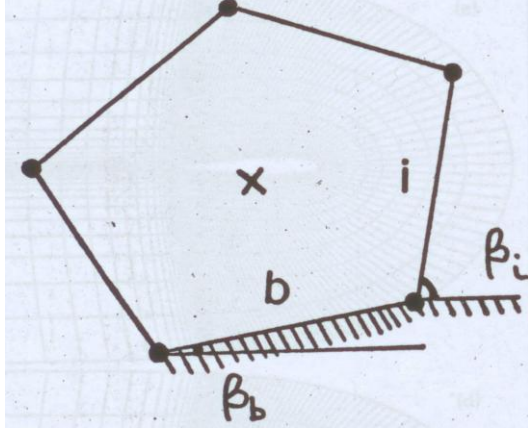


Figure 2. Scaling of artificial dissipative terms near solid boundaries, equation (27).

Many techniques have been developed for treating the dissipation terms near boundaries (reflecting conditions, various extrapolations, quadratic properties of total energy, etc.) In the present work, the problem has been circumvented, to some extent, by the simple expedient of setting equal to zero the contributions from the boundary edges. Also the contributions due to the remaining edges of cells adjacent to boundaries (both solid and outer boundaries) are scaled by a factor based on the relative angles of the edges. Following Fig. 2, the scaled contribution of the i th edge, equation (19), is taken as

$$D'_i = D_i \left| \sin \beta_i - \beta_b \right| \quad (27)$$

where β_i is the angle of the i th edge and β_b is the angle of the boundary edge of the same cell \mathbf{k} .

6. TIME DISCRETISATION

The steady-state solution is reached by an integration in time of the large system of ordinary differential equations, which may be written as

$$\frac{dW_k}{dt} = R_k \quad (28)$$

The right-hand side of the system represents the residual error (deviation from the steady-state) at each cell centre \mathbf{k}

$$R_k = -(Q_k - D_k) / \Omega_k \quad (29)$$

The integration in time of equations(28) is performed using an explicit 4-stage scheme. Since time accuracy is not important for a

steady-state solution, such schemes are selected only for their properties of stability region and damping. The following scheme is adopted for the present work

$$W^{(0)} = W^n$$

$$W^m = W^{(0)} + \alpha_m \Delta t R^{(m-1)} \quad \text{for } m=1 \text{ to } 4 \quad (30)$$

$$W^{n+1} = W^{(4)}$$

where n is the current time level, $n+1$ is the new time level and

$$R^{(m)} = -(Q^{(m)} - D^{(0)}) / \Omega \quad (31)$$

with coefficients

$$\alpha_1 = 1/4, \alpha_2 = 1/3, \alpha_3 = 1/2, \alpha_4 = 1 \quad (32)$$

In order to minimise the computation time, the expensive calculation of the dissipation function D is carried out only at the first intermediate stage(0), and this value is then frozen for the subsequent stages. As demonstrated in Ref.(7) for a scalar model equation, this procedure modifies the stability region of the scheme, but the accuracy and convergence characteristics are preserved. The above scheme is found to have a maximum CFL number for stability of $2\sqrt{2}$ when applied to the unsteady Euler equations.

The major disadvantage of explicit schemes is that the magnitude of the maximum allowable time step is restricted because of the limited stability region. Furthermore, for multi-dimensional systems of equations, the maximum time step can be evaluated only in approximate way, by analogy with the exact expression for the one-dimensional case. For grids with cells of arbitrary shape, the following form has been adopted

$$\Delta t_k = CFL \frac{\Omega_k}{\sum_{i=1}^{kedges} [|U_i \Delta y_i - V_i \Delta x_i| + c_i \sqrt{(\Delta x_i^2 + \Delta y_i^2)}]} \quad \dots\dots\dots (33)$$

7. BOUNDARY CONDITION

For inviscid flow, a condition of flow tangency is applied at solid boundaries by setting equal to zero the normal velocity flux across the boundary. The x - and y -momentum fluxes remain non-zero, due to the contributions of the pressure terms. Since the pressure is calculated at the centre of each cell,

the evaluation of the pressure at the wall remains a problem. The present method uses a simple zero-th order extrapolation procedure: the pressure at the wall is taken to be equal to the pressure at the centre of the adjacent boundary cell. Extensive numerical studies indicate that if the cells adjacent to the surface are small enough, and if the artificial dissipation terms are correctly treated, the use of this weak condition for the pressure does not have a significant influence on the accuracy of the solution.

The computational domain in which the equations are solved is finite and so the boundary conditions applied at the edge of the domain must take this into account. The requirement is that none of the outgoing waves are reflected back into the computational domain. The approach of Jameson and Baker has been followed, which comprises a locally one-dimensional theory, based on Riemann invariants, for the flow normal to the boundary.

In order to obtain an accurate solution when the circulation around the aerofoil is non-zero, the outer boundary of the computational domain has to be placed far away from the aerofoil, As shown in Ref.(3), the minimum required farfield distance may be greater than 50 chords. However, this distance can be reduced substantially by taking into account the circulation when deriving the farfield boundary conditions, Ref. (14), and this has been done in the present case.

8. ACCELERATION TECHNIQUES

Convergence to the steady-state solution can be accelerated using several standard techniques and those implemented in the present method involve the use of a local time step, together with enthalpy damping and implicit residual smoothing.

With the residual smoothing technique, the residual \mathbf{R} , equation (28), is replaced by an average of the residuals of the neighbouring cells

$$R'_k = R_k + \varepsilon \nabla^2 R_k \quad (34)$$

where ε is a smoothing coefficient, R'_k is the smoothed residual and ∇^2 is defined in equation (21). Since this explicit smoothing accelerates only slightly the convergence, an

implicit smoothing is required. The implicit form, modified for use with unstructured grids, may be written as

$$R'_k = R_k + \varepsilon \nabla^2 R'_k \quad (35)$$

so that

$$R'_k = \frac{R_k + \varepsilon \sum_{i=1}^{kedges} R'_i}{1 + \varepsilon kedges} \quad (36)$$

Since the resulting matrix of residuals is diagonally-dominant, for the values of ε of interest, this implicit system can be solved by performing several Jacobi iterations

$$R_k^{(m)} = \frac{R_k^{(0)} + \varepsilon \sum_{i=1}^{kedges} R_i^{(m-1)}}{1 + \varepsilon kedges} \quad (37)$$

where (0) refers to the unsmoothed residual, and the number of iterations required to establish the smoothed residual is small (a common value is 2). This smoothing technique allows the CFL number to be increased to 2 or 3 times the unsmoothed value.

9. RESULTS

Initial validation of the present method has been performed using several standard workshop test cases for the NACA0012 aerofoil. For inviscid flows, the entropy should be everywhere equal to the freestream value, apart from downstream of shock waves, across which there is entropy production. Thus, the deviation of the predicted entropy from the freestream value is a good indicator of the quantitative accuracy of the solution. In the Figures presented below, 'Entropy' is a non-dimensional quantity related to this difference

$$'entropy' = \frac{P / P_\infty}{(\rho / \rho_\infty)^\gamma} - 1 \quad (38)$$

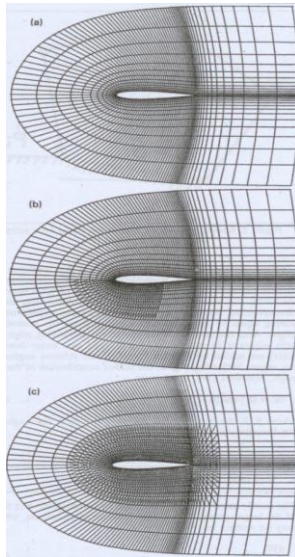


Figure 3. Partial views of computational grids for NACA 0012 aerofoil;

- (a) original structured C-grid (grid 1),
- (b) partial refinement near aerofoil (grid 2),
- (c) full refinement near aerofoil (grid 3).

Thereafter, the accuracy of predicted surface pressure distributions is assessed by comparison with several exact incompressible flow solutions for multi-element aerofoils.

9.1 NACA 0012 Aerofoil

This symmetric-section aerofoil is the most widely-used reference aerofoil for inviscid transonic flow calculations. Workshop predictions for a range of flow conditions can be found in Refs (15) and (16).

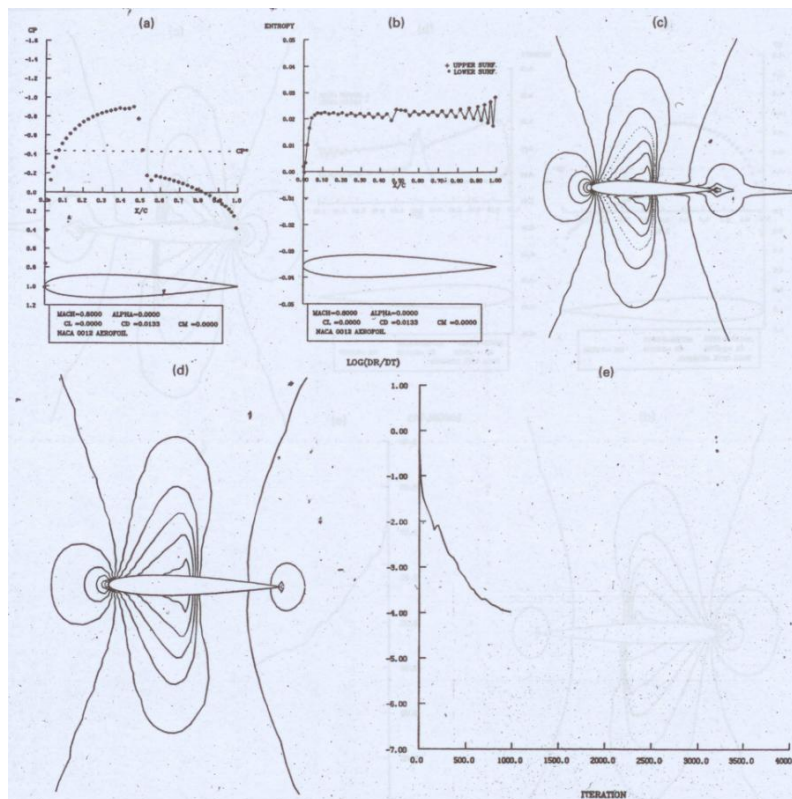


Figure 4. Results for NACA 0012 aerofoil--case 1--grid 1; (a) surface pressure distribution, (b) surface entropy distribution, (c) iso-Mach number contours, (d) iso-pressure contours, (e) convergence-history.

The first case considered was a transonic non-lifting case, with a freestream Mach number of 0.8 and incidence angle of 0° . An initial calculation of this case used the standard GAMM workshop grid, consisting of structured quadrilateral computational cells.

Figure 3(a) shows a partial view of this grid, composed of 141×20 grid-points, 100 being distributed around the aerofoil surface. The outer boundary to the computational domain is at a distance of 5 chords. Although the grid is fully-structured, it was treated in an

unstructured manner by the flow solver. The grid thus consisted of 2820 points, with 2660 computational cells and 5479 cell edges. Figure 4 shows the resulting flow-solution on this grid, which is of poor quality due to the relative coarseness of the grid, particularly in the leading-edge region. Note that a large amount of spurious (numerical) entropy is produced in this region, Fig.4(b), and is subsequently convected downstream to further corrupt the solution. The predicted drag coefficient of 0.0133 is much larger than the largest of the-workshop values quoted in Ref.(15): $0.085 < C_D < 0.010$. Also, a 'boundary-layer like' behaviour can be observed in the iso-Mach number contours near the aerofoil surface, Fig. 4(c).

In order to assess the effect of cell shape on discretisation errors and the robustness of the flow solver, a partial refinement of the initial quadrilateral grid was performed. Figure 3(b) shows that this was achieved by simply

dividing into triangles the cells around the lower surface of the aerofoil, up to a position just downstream of the shock wave. The number of grid-points remained unchanged at 2820, but 341 additional cells and cell-edges were created. A significant improvement in the flow solution on the lower surface was observed, Fig.5. In particular, the shock wave was much sharper and the behaviour of the iso-Mach number contours near the surface more nearly correct. Differences in the upper and lower surface solutions show up particularly well in the surface entropy distribution, Fig.5(b), which indicates a substantial decrease in entropy production in the leading-edge region of the lower surface. The predicted drag coefficient of 0.0118 is an improvement, presumably due to the cleaner capture of the lower surface shock wave. It is important to note that these improvements were obtained by the addition of only 341 edges to the original quadrilateral grid.

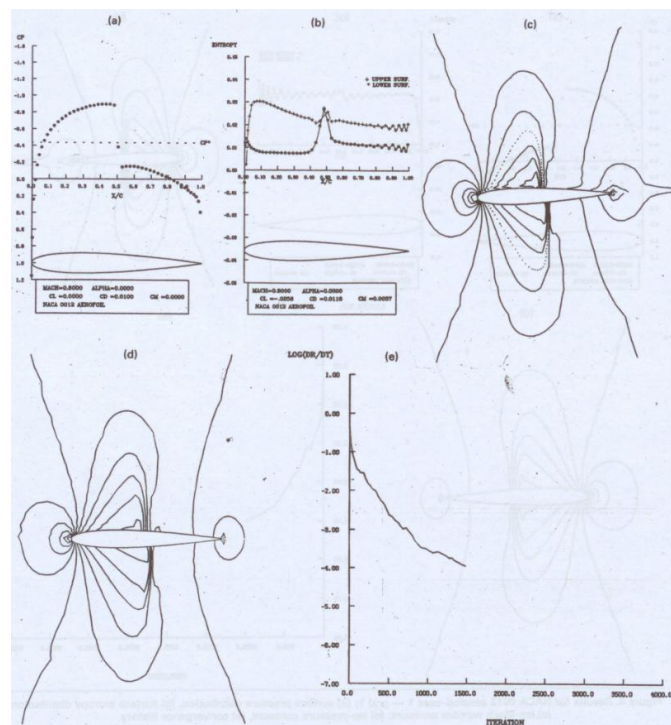


Figure 5. Results for NACA 0012 aerofoil--case 1--grid 2; (a)surface pressure distribution, (b) surface entropy distribution,(c) iso-Mach number contours, (d) iso-pressure contours, (e) convergence-history.

A further calculation for this case used a full refinement of the grid in the region around the aerofoil surface, Fig.3(c). Again, there were no additional grid-points, but a further 1298 cells and cell-edges were created (compared to the original quadrilateral grid).

Figure 6 shows that the resulting flow solution is of high quality. Spurious entropy production in the leading-edge region is essentially zero, and the shock waves are captured in only two or three computational cells. The predicted drag coefficient of 0.0100 is now comparable

with the GAMM workshop predictions. Finally, the iso-Mach number and iso-pressure contours are smooth in the interface region

between the refined triangular cells and the original quadrilaterals.

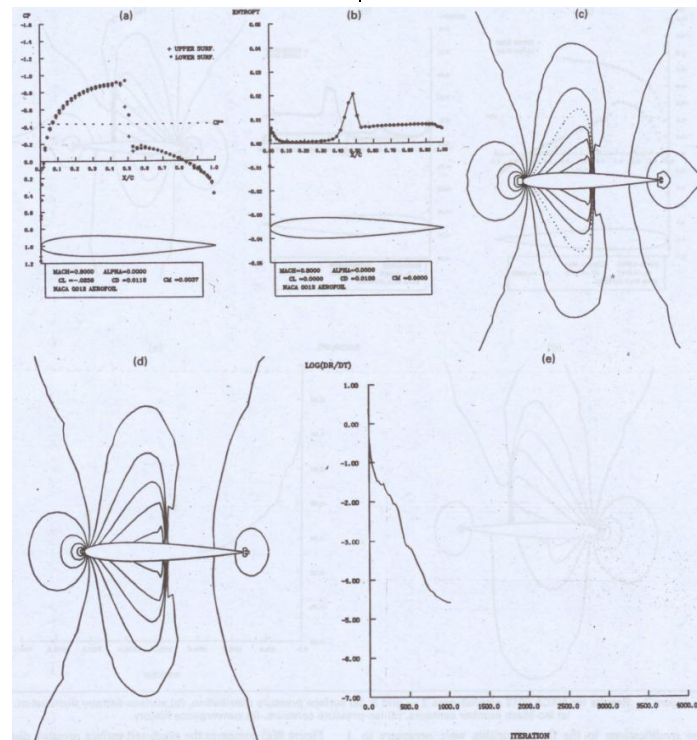


Figure 6. Results for NACA 0012 aerofoil--case 1--grid 3; (a)surface pressure distribution, (b) surface entropy distribution,(c) iso-Mach number contours, (d) iso-pressure contours, (e) convergence-history.

Figure 7 shows predictions for a second NACA 0012 aerofoil case, at a freestream Mach number of 0.8 and incidence angle of 1.250. The calculation employed the fully-refined grid shown in Fig. 3(c). The solution quality is good, in general, and includes a weak shock wave on the lower surface at around 30% chord. However, there is still some spurious entropy production in the leading-edge region, indicating that a further refinement of the grid in this region is necessary. Nevertheless, the predicted lift and drag coefficients of 0.340 and 0.0228 respectively are in good agreement with independent results for this case, on a variety of finer computational grids: $0.346 < C_L < 0.373$ and $0.0221 < C_D < 0.0244$.

9.2 Multi-element Aerofoils

Having validated the present flow algorithm for single aerofoils, the method was then applied to predicting the inviscid flow around the multi-element aerofoil configurations associated with mechanical high-lift systems. The main problem with such calculations concerns the generation of a suitable computational grid around the geometry, the flow domain being multiply-connected. For the results presented below, completely unstructured grids consisting of triangular cells were generated using the approach of Weatherill, based on a Delaunay triangulation of a given set of gridpoints. Note that, after generation of the computational grid, no modifications to the flow algorithm were necessary to compute the multi-element aerofoil cases given below.

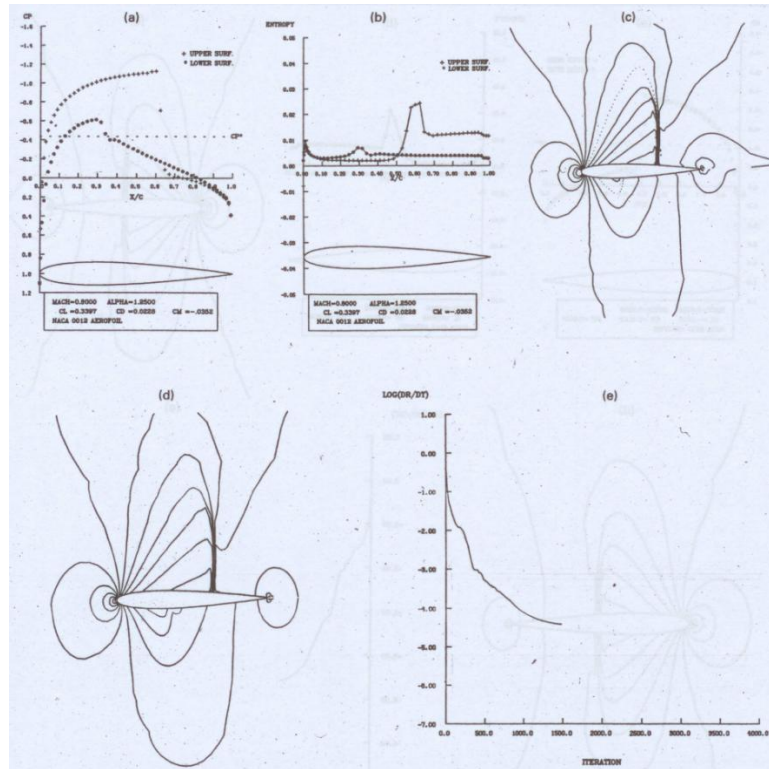


Figure 7. Results for NACA 0012 aerofoil--case 2--grid 3; (a)surface pressure distribution, (b) surface entropy distribution,(c) iso-Mach number contours, (d) iso-pressure contours, (e) convergence-history.

The first case consisted of a 3-element aerofoil, in a leading-edge slat and trailing-edge flap configuration. Figure 8 shows the geometry, together with partial views of the unstructured grid. The grid was composed of 3540 points, forming 6544 cells with 9996 cell-edges. There were 96 surface grid-points on the main aerofoil element, with 85 each on the slat and flap. An exact incompressible potential flow solution for this geometry has been computed by Suddhoo and Hall, by extending the conformal mapping and method of images approach of Williams. The solution corresponds to a freestream Mach number of zero and an incidence angle of 200° . The present calculation was made at a Mach number of 0.125, since the compressible flow algorithm, in its current form, is not applicable to completely incompressible flow conditions.

Figure 9(a) compares the predicted surface pressure distribution with the exact potential flow solution. The main differences are on the

upper surfaces of the first two aerofoil elements. Numerical experiments indicated that these differences were due to the compressibility of the present algorithm, rather than being associated with a lack of grid resolution. Note the large suction peaks in the leading-edge regions of all the aerofoil elements. In particular, the flow around the slat is almost sonic in this region, despite the very low freestream Mach number. Therefore, it seems that the present compressible flow solution is the more physically realistic inviscid solution. Figure 9(c) indicates that the level of spurious entropy is everywhere less than 0.005 on the aerofoil surface. As an independent check on the accuracy of the present predictions. Fig.9(b) shows a comparison with a solution using the cell-vertex Euler algorithm of Jameson et al, on exactly the same computational grid. There is a very satisfactory level of agreement between the two predictions.

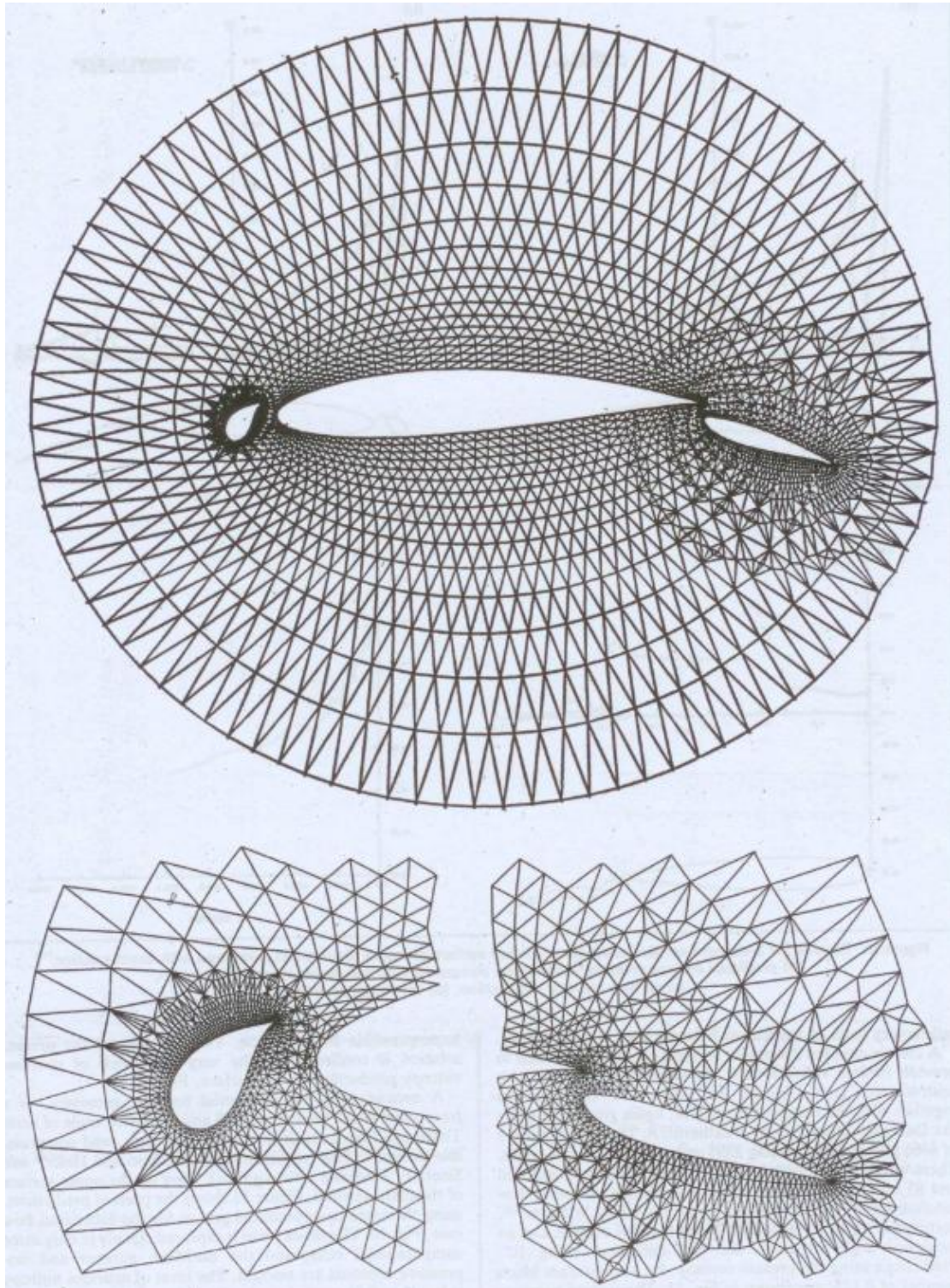
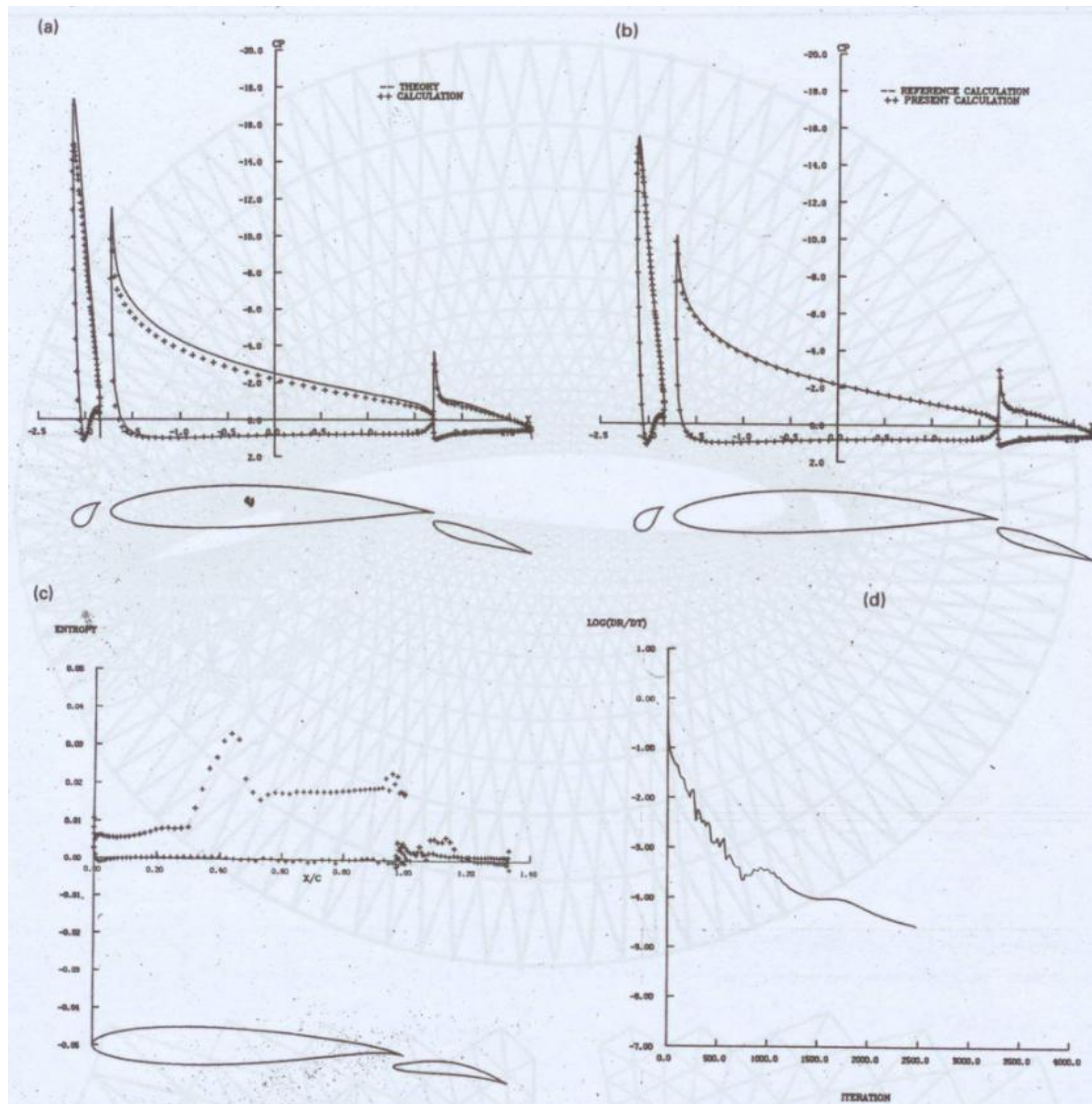


Figure 8. Partial views of computational grid for 3-element aerofoil of Suddhoo and Hal-case B.



Figur9. Results for 3-element aerofoil case;

- (a) predicted surface pressure distribution compared with exact solution,
 (b) predicted surface pressure distribution compared with cell-vertex algorithm solution,
 (c) surface entropy distribution,(d)convergence history.

A closely-coupled 2-element aerofoil geometry was used to provide further validation of the calculation method with unstructured grids. Figure.10 shows the configuration together with the computational grid, again generated using the Delaunay algorithm of Weather11. The grid consisted of 4466 grid-points, forming 8595 cells with 13061 cell-edges. There were 128 grid-points on the surface of the main aerofoil and 85 on the flap. An exact incompressible potential flow solution for this geometry has been derived by Williams, corresponding to a freestream Mach number of zero and an incidence angle of zero, the flap deflection

being 100. Predictions using the present method, for a freestream Mach number of 0.125, are shown in Fig.11. The surface pressure distribution is in excellent agreement with the exact incompressible flow solution. The accuracy of the present solution is confirmed by the very low levels of spurious entropy production on the surface, Fig.11(b).

A second case was computed for this geometry, at a freestream Mach number of 0.58 and incidence angle of zero. These conditions result in supercritical flow, and compressible potential flow calculations by Suddhoo and Hall and Sinclair indicate a strong shock wave on the upper surface of the

main aerofoil. Figure 12 shows the present predictions, using the same computational grid as for the subcritical flow case, Fig. 10. The shock wave is captured cleanly in only three computational cells, and the iso-Mach number and iso-pressure contours are smooth. The level of spurious entropy is less than 0.01 around the leading edge of the main aerofoil, and could be reduced by further refinement of the grid in this region. Figure 12 indicates the ability of the present method to predict complex transonic inviscid flows in a relatively straightforward manner.

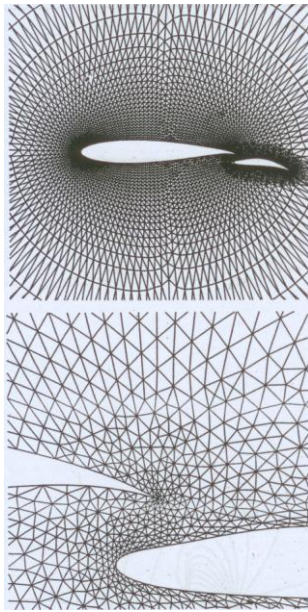


Figure 10. Partial views of computational grid for 2-element aerofoil of Williams-case B.

All the above calculations were performed using the following flow-algorithm coefficients:

$CFL=8.4$, $0.5 < k^{(2)} < 0.6$, $k^{(4)} = 0.007$, $\varepsilon = 0.5$. The code has been implemented on an Alliant FX/3 mini-supercomputer and the typical CPU time for a calculation involving local time-stepping, enthalpy damping and implicit residual smoothing is $0.33E-3$ seconds/iteration/edge.

10. CONCLUSIONS

A method for the steady-state solution of the two-dimensional Euler equations on unstructured grids has been presented. The finite-volume spatial discretisation technique

is applied in a general formulation, so that the present algorithm allows the use of arbitrary polygonal cell shapes.

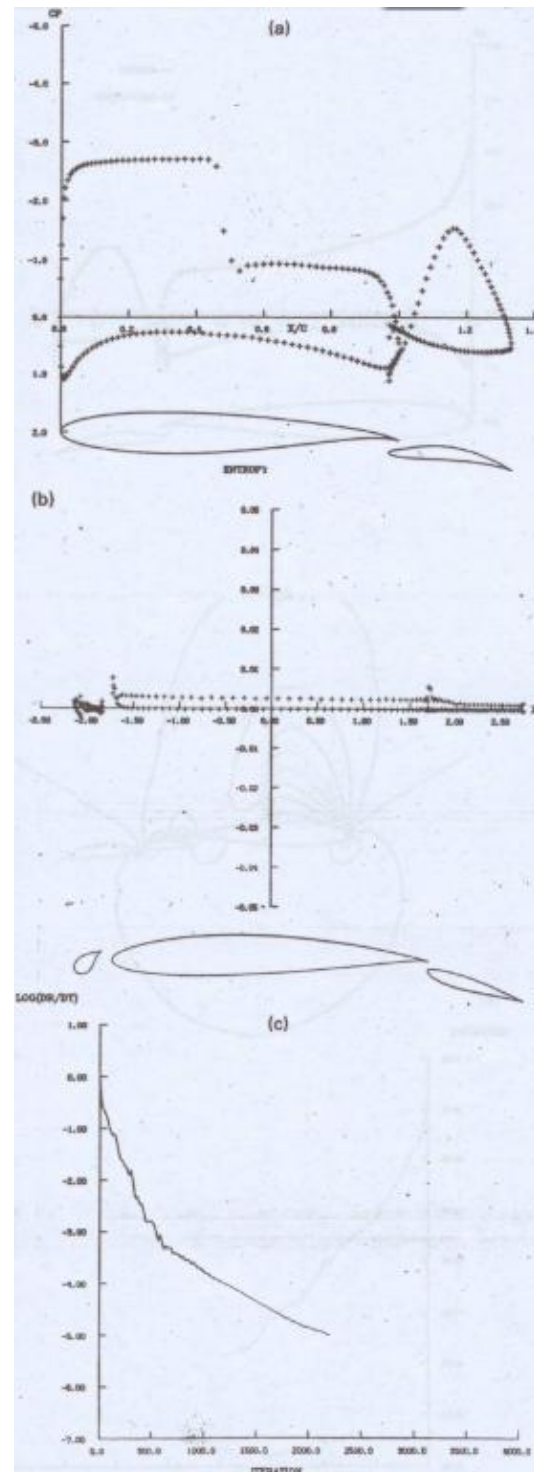


Figure 11. Results for 2-element aerofoil-subcritical flow;(a) predicted surface pressure distribution compared with exact solution,(b) surface entropy distribution, (c) convergence history.

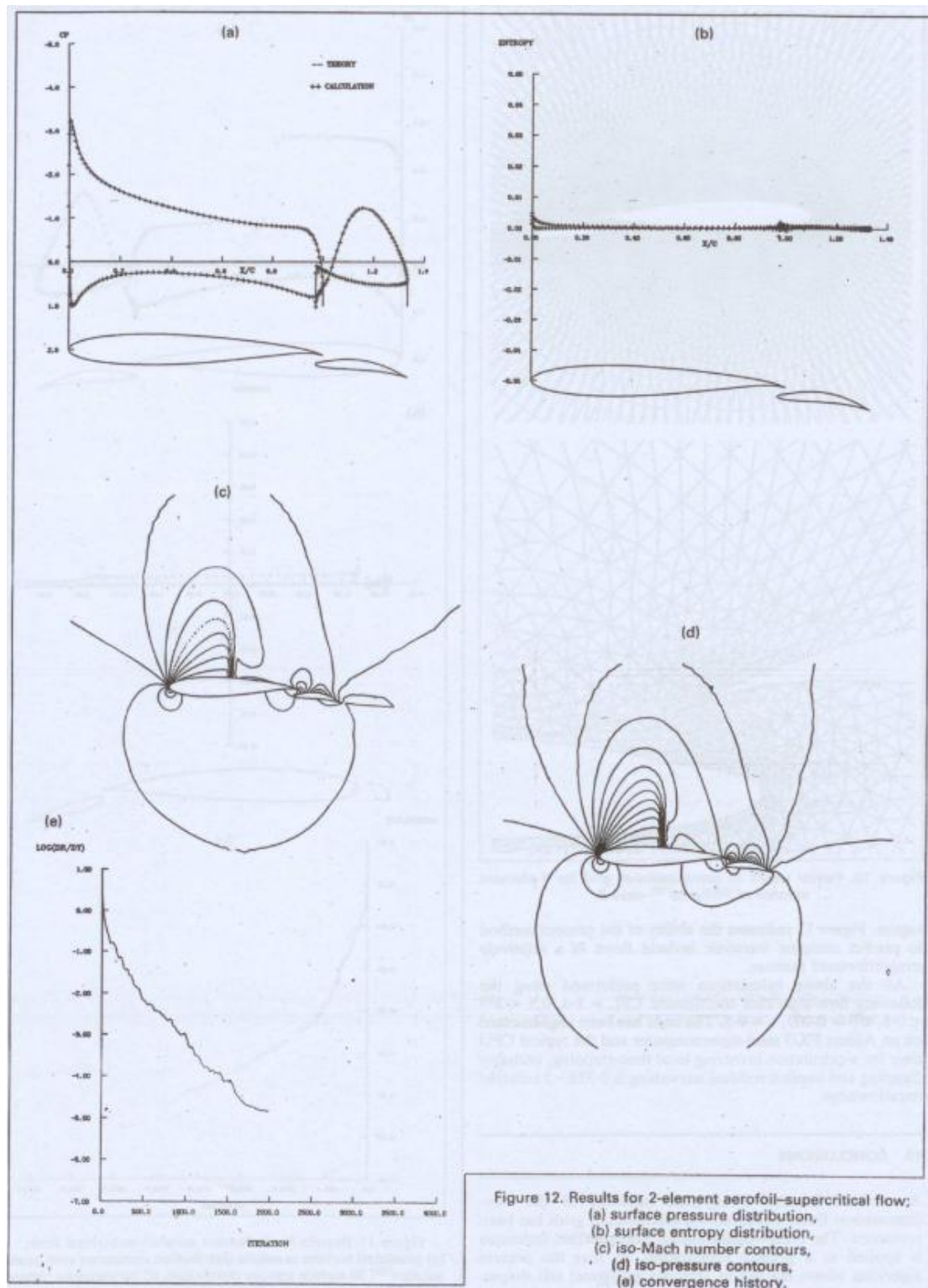


Figure 12. Results for 2-element aerofoil-supercritical flow;
(a) surface pressure distribution,
(b) surface entropy distribution,
(c) iso-Mach number contours,
(d) iso-pressure contours,
(e) convergence history.

Figure 12. Results for 2-element aerofoil-supercritical flow;

- (a) surface pressure distribution, (b) surface entropy distribution, (c) iso-Mach number contours,
(d) iso-pressure contours, (e) convergence history

The steady-state solution is reached by integrating the unsteady form of the equations in time using an explicit multi-stage procedure.

The convergence can be accelerated by means of some standard acceleration techniques. The ability of the present method to treat arbitrary

grids and complex geometries has been demonstrated. The generality of the present approach would enable the implementation of flow refinement techniques or mesh adaptive procedures without any changes in the basic algorithm.

The present method is to be the starting-point for the development of a method to predict compressible viscous flow around complex geometries, such as multi-element aerofoils, solving the Reynolds-averaged

Navier-Stokes equations. However, in order to minimise the influence of the artificial viscosity on the natural viscosity of the flow, additional investigation of the numerical dissipative terms is required. Also, the use of unstructured grids will require a generalised approach to turbulence modelling, probably involving a transport-equation type model. These various issues concerning viscous flow prediction are currently under investigation.